OBSERVING "INTEGRATING" VARIABLES IN THE OCEAN

Douglas S. Luther
Department of Oceanography, School of Ocean and Earth Science and Technology
University of Hawaii at Manoa, Honolulu, Hawaii 96822

Alan D. Chave
Department of Geology and Geophysics, Woods Hole Oceanographic Institution
Woods Hole, Massachusetts 02543

ABSTRACT

Some physical variables are natural spatial integrals of oceanic water motion or state properties. Observation of these variables permits isolation of physical processes that might otherwise be difficult to examine because of the superposition of many phenomena at one place. Independent of a particular physical model, observations of such integrating quantities frequently enable direct determination of relatedness between variables at different locations, and direct determination of causality, while more traditional point observations may fail to find such relationships. Furthermore, integral quantities such as volume and heat transport, which are now being studied with great fervor because of their climatic importance, are likely more accurately estimated using observations of "integrating" variables than using a set of point measurements. Examples of integrating types of variables, such as horizontal electric fields, vertical acoustic travel time and bottom pressure, are used to demonstrate the ideas above with examples drawn from the study of (a) atmospherically forced, mesoscale motions, and (b) the volume and heat transports of the Gulf Stream.

INTRODUCTION

At any particular location in the oceans, the sub-inertial water motions and fluctuations of state properties are likely to be due to a superposition (and, possibly, interaction) of a variety of phenomena that each have specific and different balances between acceleration, advection, Coriolis forces, pressure, dissipation, external forcing, and so on. Time-dependent boundary layers exist as a result of property fluxes to and from the atmosphere and earth. Semi-permanent meso- and gyre-scale currents (O(100 km) and O(1000 km), respectively) of the "general circulation" are forced by the winds and property fluxes, and, through instabilities, produce meso- and gyre-scale variability in the form of meandering currents, coherent vortices, radiated waves, and so on. Meso- and gyre-scale variability can also be directly driven by the atmosphere. Each of these, and many other unlisted phenomena, exist at a variety of space scales for each time scale, so that they overlap each other not only in physical space and time, but in frequency and wavenumber space as well.

To decipher the ocean's physics, it is often preferable to examine a single phenomenon at a time. Then one has to consider "contamination" from the other phenomena that would inhibit, for instance, direct detection of relatedness among oceanic variables and between oceanic and atmospheric variables.

There are of course a number of strategies for isolating particular phenomena in order to study their kinematics and dynamics. Sometimes, time series of variables are all that is needed to separate phenomena according to their characteristic frequencies. Other times, spatial information is needed, which raises the cost and difficulty of a field experiment, but which allows discrimination of wavenumbers or principal components and thereby possible discrimination of different processes. Frequently, experiments are designed so that there is a reasonable certainty that the phenomenon to be studied dominates all other processes. However, there are many instances when this cannot be accomplished. In these cases, observations are usually compared with model output visually, graphically, statistically, or through dynamical parameter estimation. Such comparisons can lead to the identification of the quality of the dynamical hypotheses as a function of frequency and/or wavenumber. It is not unusual for experiments to be designed to take advantage of most if not all of the strategies above.

The purpose of this note is to point out that there now exists an additional observational strategy, most components of which are rather new to oceanography, for isolating phenomena that are large scale in the vertical and/or horizontal. This strategy is based on the measurement of integrating variables. The spatial filtering inherent in these variables frequently enables statistical confirmation of important large scale kinematic and dynamic relationships which might otherwise go undetected except with a formidably large array of point measurements. Yet, in deference to the theme of this workshop, it must be acknowledged that isolating large scale phenomena does not imply that the phenomena observed, or statistics of these phenomena estimated from integrating variables, are homogeneous over large scales as well. This inhomogeneity complicates, if not invalidates, the application of many statistical procedures that assume homogeneity.

We define integrating variables as those that are natural spatial integrals of oceanic water motion or state properties. Table 1 lists a few of the more important integrating variables being observed today. These integrating variables are ones that by their very nature tend to filter out the shorter spatial scale variability. The techniques we'll discuss in this note are those whose usefulness is well-established and which offer the advantage of cost-effectiveness. In addition, these techniques may have greater accuracy in comparison to using a suite of point measurements when the ultimate goal of an investigation is the measurement of an integral quantity such as volume transport.

Table 1. Examples of Integrating Variables.

Variable	Principal component of integrand	References
Horizontal electric fields at a point	Conductivity-weighted horizontal water velocity, from seafloor to sea surface	Sanford (1971) Chave & Luther (1990) Luther et al. (1991)
Voltages across fixed horizontal distances (typically, using abandoned undersea telephone cables)	Conductivity-weighted horizontal water velocity (one component only), from seafloor to sea surface over a fixed horizontal distance	Larsen & Sanford (1985) Larsen (1992) Chave et al. (1992b)
Vertical acoustic travel time	Inverse sound speed from seafloor to sea surface	Watts & Rossby (1977) Pickart & Watts (1990)
Bottom pressure	Horizontal water velocity near the seafloor, over a fixed horizontal distance	Brown et al. (1975) Whitworth & Peterson (1985)
Horizontal acoustic travel time (acoustic thermometry)	Inverse sound speed along horizontal, depth-varying ray paths	Munk & Forbes (1989)
Reciprocal acoustic travel time	Water velocity along horizontal, depth-varying ray paths	Worcester (1977) Worcester et al. (1991)
Orientation of the earth's axis of rotation	Global mass distribution (especially in hydrologic reservoirs)	Chao (1988) Eubanks (1993)
Rotation rate of the earth	Global atmospheric angular momentum (principally, fluctuations in zonal winds)	Hide & Dickey (1991) Eubanks (1993)

Measurement of integrating variables allows the investigator to focus immediately on a specific region of wavenumber space, without the "contamination" of shorter scale variability that may depend on processes other than the one being sought. Furthermore, such restriction of the wavenumber space may enable the detection of properties (like spatial coherence or air-sea coherence) that tend to zero as the wavenumber bandwidth increases and may provide more useful constraints for numerical model simulations than do point measurements.

In the sections that follow, we will describe applications of three of the more underutilized, yet most cost-effective, integrating variables listed in Table 1, including point measurements of horizontal electric fields (HEFs), vertical acoustic travel time (VATT), and bottom pressure (P_b). We will show how observations of HEFs and P_b in the Barotropic, Electromagnetic and Pressure Experiment (BEMPEX) provided definitive evidence of the existence of gyre-scale motions that are directly forced by sea surface winds. Horizontal electric field data from the Synoptic Ocean Prediction (SYNOP) experiment will be shown that suggest the greater accuracy of these integrating variables in estimates of volume transport. And, we will outline the potential utility of combining HEF and VATT observations to obtain nearly direct estimates from the seafloor of heat transport and the gravest vertical structures of horizontal currents and temperature fluctuations.

HORIZONTAL ELECTRIC FIELDS

Motional electromagnetic induction is now theoretically well understood in certain idealized settings (e.g., Sanford, 1971; Chave and Luther, 1990). Assuming distant continental boundaries and a flat seafloor with laterally homogeneous conductivity, then for the low-frequency limit where the aspect ratio of ocean currents is small, where the effect of self induction is weak, and where the vertical velocity can be neglected in comparison with the horizontal velocity, it can be shown that the point HEFs are related to horizontal water velocity by

$$\vec{E}_h(x,y,t) = CF_z k \times < \vec{v}_h(x,y,t) >^* + \frac{\vec{J}^*}{\sigma} + \vec{N}(x,y,t), \tag{1}$$

where

$$< \vec{v}_h(x,y,t) >^* = \frac{\int_{-H}^{0} dz\, \sigma(x,y,z,t)\, \vec{v}_h(x,y,z,t)}{\int_{-H}^{0} dz\, \sigma(x,y,z,t)} \tag{2}$$

and is called the conductivity-weighted, vertically averaged (CWVA) water velocity; $\vec{v}_h(x,y,z,t)$ is horizontal water velocity; $\sigma(x,y,z,t)$ is seawater electrical conductivity; F_z

is the vertical component of the geomagnetic field; and $H(x,y)$ is ocean depth. The scale factor C depends on $\sigma(z \le -H)$; C can be estimated by intercomparisons, but extensive geophysical evidence suggests that $C = 0.95 \pm 0.05$ almost everywhere in the deep oceans (e.g., Chave and Luther, 1990). A noise term $\vec{N}(x,y,t)$ is composed of externally produced (i.e., in the ionosphere and magnetosphere) electromagnetic fields that dominate for periods shorter than a few days but are negligible at longer periods (e.g., Chave et al., 1989).

Locally and non-locally produced electric currents are represented by $\vec{J}^*$. Given usual oceanic scales of motion at sub-inertial periods (greater than half a pendulum day), locally produced electric currents are theoretically negligible if the bottom is flat (Chave and Luther, 1990) or the flow is aligned along isobaths (Stephenson and Bryan, 1992). Local generation of $\vec{J}^*$ may be sufficient to inhibit accurate estimation of ocean water currents with electric fields only where the currents cut across isobaths and then only if the underlying sediments are relatively non-conductive (Larsen, 1992; Stephenson and Bryan, 1992). Meandering of a narrow current like the Gulf Stream can theoretically produce non-zero $\vec{J}^*$ outside of the stream boundaries (the principal example of non-local generation of $\vec{J}^*$), which theoretically could be a large noise relative to the electric field signal induced by the smaller water currents there. However, Sanford (1986) has pointed out that observations have shown $\vec{J}^*/\sigma$ to be small [yielding errors of O(1 cm/s)] and generally negligible. And our own work with the SYNOP data has shown that the best agreement between the moored current meter data and the horizontal electrometer data occurs where the currents are moderate to weak, resulting in no detectable $\vec{J}^*$. Therefore, in the following, $\vec{J}^*$ is ignored.

Dropping the horizontal dependences and letting $\sigma(z,t)$ equal a vertical average part plus a residual, i.e.,

$$\sigma(z,t) = <\sigma(t)> + \hat{\sigma}(z,t), \text{ where } <\sigma(t)> = \frac{1}{H}\int_{-H}^{0} dz\, \sigma(z,t), \tag{3}$$

then Eq. 2 becomes

$$<\vec{v}_h(t)>^* = <\vec{v}_h(t)> + \frac{\int_{-H}^{0} dz\, \hat{\sigma}(x,t)\,\vec{v}_h(x,t)}{H <\sigma(t)>}. \tag{4}$$

The first term on the right hand side (RHS) of Eq. (4) is just the vertical average of horizontal water velocity (or depth-normalized transport per unit width). The second term on the RHS of Eq. (4) is a small contribution because seawater conductivity is a weak function of depth. Note that $|\hat{\sigma}(z,t)| \ll <\sigma(t)>$; $<\sigma(t)>$ is always greater than 3 Siemens m^{-1}; to a good approximation, $\sigma(z,t) = 3.0 + 0.09T(z,t)$ Siemens m^{-1}, where $T(z,t)$ is

unless the horizontal currents are strong and baroclinic (i.e., have large vertical shear). Assuming low-frequency motions so that $\vec{N}(t)$ can be ignored, and using Eq. (4), the components of Eq. (1) in the northern hemisphere become

$$\frac{E^u_{-y}(t)}{C|F_z|} = <u(t)> + \frac{1}{H}\int_{-H}^{0} \frac{\hat{\sigma}(z,t)}{<\sigma(t)>} u(z,t)\,dz, \tag{5a}$$

$$\frac{E^v_{x}(t)}{C|F_z|} = <v(t)> + \frac{1}{H}\int_{-H}^{0} \frac{\hat{\sigma}(z,t)}{<\sigma(t)>} v(z,t)\,dz, \tag{5b}$$

where the subscript on E denotes the direction in which that term is positive and the superscript indicates the horizontal water velocity component to which it is proportional. Clearly, the HEFs are integrating variables in the sense defined in the introduction, being proportional to the vertical average of horizontal water velocity plus a small "contamination" due to conductivity. The conductivity contribution is negligible if conductivity is independent of depth in the ocean (as it is at very high latitudes) or if the horizontal water velocity has little vertical shear (as frequently occurs at mid- to high-latitudes).

Normal Modes

To elucidate further the relationships in Eq. (5), it is useful to expand the various quantities in terms of the dynamical normal modes. While any complete basis set could be used, the dynamical normal modes have a vertical dependence that permits rapid convergence of the expansions of horizontal velocity and seawater conductivity and temperature. Despite the fact that the dynamical normal modes are obtained from the equations of motion by various simplifying assumptions such as no mean flow and linearity, in using these modes here we are not making any assumptions about the underlying dynamics of the quantities being observed. The modes are simply the most convenient basis set for our purposes.

The dynamical modes are obtained from the equations of motion by assuming no mean flow, mean stratification in hydrostatic balance, and a flat bottom. With horizontal velocity and pressure proportional to $\phi_i(z)$, and vertical velocity and density perturbations proportional to $\theta_i(z)$, the equations for Boussinesq linear waves (small perturbations) then separate into sets of equations for the horizontal/time dependence and vertical dependence. Specifically, with

$$\begin{Bmatrix} \vec{v}_h(z,t) \\ p(z,t)/\rho_* \end{Bmatrix} = \sum_{i=0}^{\infty} \begin{Bmatrix} \vec{a}_{h,i}(x,y,t) \\ d_i(x,y,t) \end{Bmatrix} \phi_i(z) \tag{6a}$$

and

$$\begin{Bmatrix} w(z,t) \\ \rho'(z,t)g/N^2(z) \end{Bmatrix} = \sum_{i=0}^{\infty} \begin{Bmatrix} f_i(x,y,t) \\ g_i(x,y,t) \end{Bmatrix} \theta_i(z) \tag{6b}$$

where $\rho = \rho_* + \overline{\rho}(z) + \rho'(z,t)$ and $N^2(z) = -\frac{g}{\rho_*}\frac{d\overline{\rho}}{dz}$, then ϕ_i and θ_i satisfy

$$\phi_i = \frac{d\theta_i}{dz} \text{ and } \frac{d\phi_i}{dz} = -\frac{N^2}{\gamma_i^2}\theta_i \tag{6c}$$

with the boundary conditions

$$\theta_i = 0 \text{ or } \frac{d\phi_i}{dz} = 0 \text{ at } z = -H, \tag{6d}$$

$$\frac{d\theta_i}{dz} - \frac{g}{\gamma_i^2}\theta_i = 0 \text{ or } \frac{d\phi_i}{dz} + \frac{N^2}{g}\phi_i = 0 \text{ at } z = 0. \tag{6e}$$

Equations (6c) are solved numerically with the appropriate boundary conditions to produce the vertical structure functions and eigenvalues, γ_i^2. The structure functions are orthogonal and are normalized so that

$$\frac{1}{H}\int_{-H}^{0} \phi_i \phi_j \, dz = \delta_{ij}. \tag{6f}$$

This normalization means that the ϕ_i are non-dimensional, while the θ_i have dimensions of length. We now have a complete orthonormal basis set for describing any quantity that varies with depth. The fact that these modes are "tuned" to the depth-dependences of real oceanographic variables makes them very useful, since it means expansions in terms of these modes should converge rapidly. For our purposes in this section, it is not important what assumptions were used to obtain the vertical structure equations in Eq. (6c).

Let's now expand conductivity in terms of the dynamical modes, viz.,

$$\frac{\hat{\sigma}(z,t)}{<\sigma(t)>} = \sum_{i=1}^{\infty} s_i(x,y,t)\phi_i(z), \tag{7}$$

where the i=0 (barotropic) mode has been dropped since the vertical average of $\hat{\sigma}$ is zero. Substituting this expression and those in Eq. (6a) into Eq. (5), and truncating after mode number 1, yields

$$\frac{E_{-y}^{u}(t)}{C|F_z|} \approx a_{x,0} + s_1 a_{x,1}, \tag{8a}$$

$$\frac{E_{x}^{v}(t)}{C|F_z|} \approx a_{y,0} + s_1 a_{y,1}, \tag{8b}$$

The truncation in Eq. (8) is quite reasonable given the expected decrease in modal current amplitudes with increasing mode number, and given the examples in Table 2 of mean s_i, calculated using Levitus (1982) data to compute structure functions and conductivity profiles. Table 2 suggests that in polar oceans and in the mid-latitude Pacific the conductivity-weighting contribution to the electric field is completely trivial. Using a year of electric field and current meter mooring data, Luther et al. (1991) have shown the validity of Eq. (5) in a region of the mid-latitude North Pacific with weak mean currents and weak baroclinic eddy activity. In that location, the conductivity-weighting contribution to the electric field was completely trivial.

Table 2. Expansion coefficients for conductivity from Eq. (7).

	s_i		
Mode (i)	32.5°N Atlantic	42.5°N Pacific	57.5°S Atlantic
1	0.119	0.017	-0.004
2	-0.014	0.021	-0.009
3	-0.012	-0.002	-0.004
4	0.008	0.008	-0.001

On the other hand, in the mid-latitude North Atlantic, equal amplitudes of the barotropic (i=0) and first baroclinic (i=1) modes of current imply a ~12% relative contribution to the electric field from the last term on the RHS of Eq. (5). Rossby (1987) found first baroclinic mode amplitudes up to 70% greater than barotropic mode amplitudes in the Gulf Stream at 73°W, with very small second and third baroclinic mode amplitudes. Consequently, in the Gulf Stream we can expect up to 20% conductivity-weighting contributions to the electric field due to the first baroclinic mode of current. In fact, our work with SYNOP data has shown occasional conductivity-weighting contributions up to 30%, although the mean contribution is <15%.

The variation of conductivity with depth in the oceans (e.g., Luther et al., 1991) suggests dominance of the first baroclinic mode in the conductivity contribution to Eq. (5), which allows the use of another integrating measurement, vertical acoustic travel time, to estimate first baroclinic mode current and temperature amplitudes in order to remove the conductivity contribution from the HEF. This procedure is outlined later.

Horizontal Electrometer (HEM) Versus Mooring Estimates of Transport

In deployments of seafloor HEMs to date, where comparison of HEM estimates of the vertically averaged horizontal water velocity, $< \vec{v}_h(t) >$, with current meter mooring

estimates of the same quantity have been possible, the HEM estimates have proven to be more accurate. These results provide an example of how measurement of an integrating variable provides a more accurate estimation of oceanic behavior than can be accomplished with a suite of conventional point measurements. In this specific case such accuracy has significant importance to climate studies that rely on estimates of transport (which is directly proportional to horizontal integrals of $H< \vec{v}_h(t) >$ for determining the world ocean's role in climate fluctuations.

The first HEM vs. mooring comparison of $< \vec{v}_h(t) >$ estimates was produced by Luther et al. (1991) from data collected during BEMPEX, an experiment that deployed a large number of HEMs and pressure gauges in the North Pacific to study direct atmospheric forcing of gyre-scale eddies (the results of which are discussed further below). The accuracy of the HEM estimates of $< \vec{v}_h(t) >$ was corroborated by current estimates made by reciprocal tomography, which is based on measuring reciprocal acoustic travel time differences (Table 1). The inaccuracy of the current meter mooring estimates was attributed primarily to stalling of the current meter rotors in the weak flows below 1000 meters depth. Another electrometer-mooring comparison presented below comes from the opposite extreme for oceanic flows, i.e., from the Gulf Stream which has strong currents at all depths so that rotor stalling is not expected to be a problem.

The Office of Naval Research provided funds for us (with Jean Filloux) to deploy four of Filloux' seafloor HEMs (Filloux, 1987) next to current meter moorings during the last year ('89-'90) of the SYNOP experiment in the Gulf Stream. The HEMs were deployed in an array centered around 37.5°N, 68.5°W, at depths near 4700 m. Near each HEM were sub-surface moorings deployed by J. Bane, T. Shay, R. Watts, and W. Johns, carrying current meters at nominal depths of 400 m, 700 m, 1000 m and 3500 m.

The LHSs of Eqs. (5a) and (5b) were obtained from the HEM data using C=0.95, as per estimates of C made by Sanford et al. (1985) in the western North Atlantic, and using an appropriate estimate of F_z for the time and location of the experiment, while the RHSs were estimated from the mooring data. The latter estimation included extrapolation of $\vec{v}_h$, temperature and pressure to a fictitious nominal 100-m depth, conversion of pressure to 'depth,' and estimation of conductivity using temperatures and a climatological temperature/salinity relation in an empirical formula. The currents and conductivities at the four real and one "fictitious" instruments were trapezoidally integrated, taking into account the time dependence of the depths of the instruments. The time series thus obtained, representing opposite sides of Eq. (5), are highly coherent, as shown in Figure 1.

While the coherence in Figure 1 is very encouraging, and the rms differences between the estimates of the LHS and RHS of Eq. (5) are no larger for instance than what has been considered very good agreement for testing schemes to remove the effects of mooring motion from current meter data (e.g., Hogg, 1991; Cronin, 1991), examination of the

individual time series (not shown) indicates that the LHS of Eq. (5) consistently has a greater magnitude than the RHS. That there is a systematic under-estimation of current by the mooring data, or an over-estimation by the HEM data, is most easily seen by casting the data in terms of a Gulf Stream coordinate system, rather than a geographic coordinate system, since the Gulf Stream position and direction vary with time.

Daily locations of the temperature front of the Gulf Stream (provided by R. Watts and W. Johns) were determined from an array of Inverted Echo Sounders (IESs) that measure VATT. These locations permitted estimation of the cross-stream positions of the moorings every day. Gulf Stream directions at each mooring were determined from the 400-1000 m shear. Daily estimates of Eq. (5) were then rotated into these Gulf Stream coordinates.

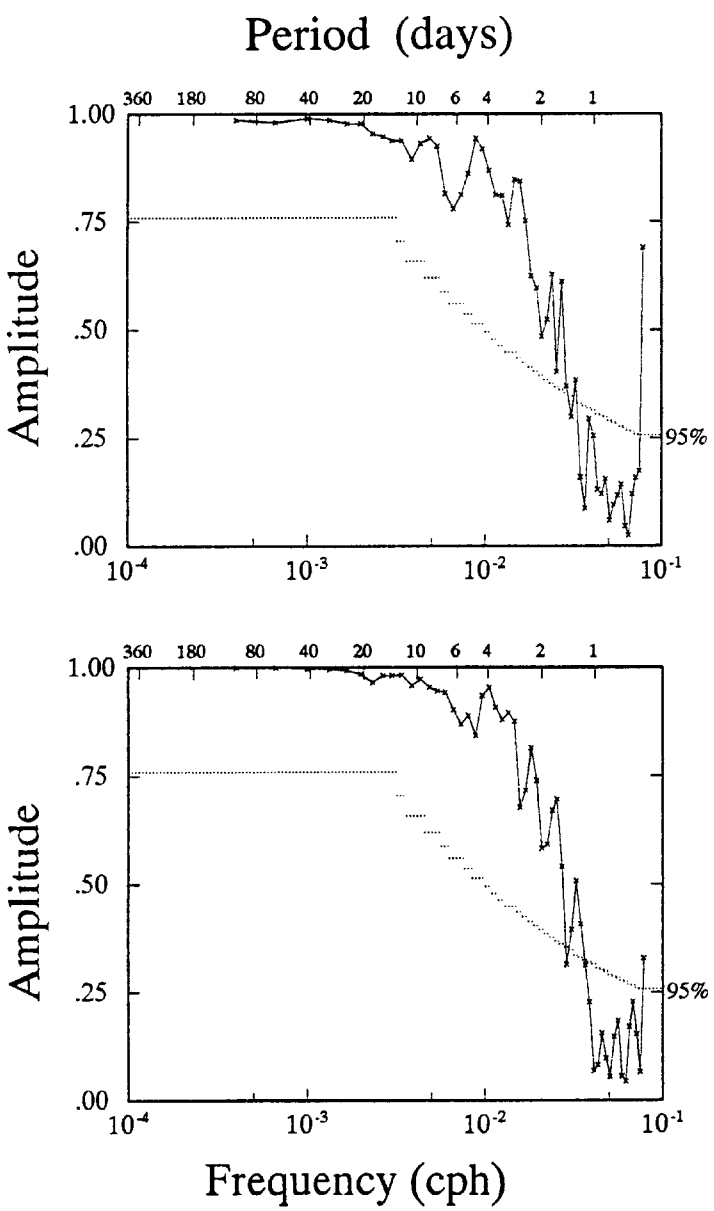

To put the problem in a more interesting context, the conductivity contribution term (the last term on the RHS of Eq. (5)) was moved to the LHS of Eq. (5). Now we can compare mooring estimates of vertically averaged water velocity, $< \vec{v}_h(t) >$, with HEM estimates of the same quantity (that incorporates a small

Figure 1. Coherence amplitudes between electrometer and mooring estimates of conductivity-weighted, vertically averaged water velocity (left and right hand sides of Eq. (5), as described in the text). Top is for zonal currents (Eq. (5a). The 95% level of no significance is indicated. Every other point plotted is independent due to a 50% overlap of frequency band-averaging.

mooring-derived conductivity correction), all cast in terms of Gulf Stream coordinates. The results for a single mooring are shown in Figure 2, along with the difference (error) between the two estimates. (Note that the error is not dependent upon which side of Eq. (5) we place the conductivity correction term.) The results in Figure 2 typify the comparisons made at other HEM locations. Integrating the estimates in Figure 2 across the stream results in a ~30% higher estimate of total transport from the HEM than from the mooring. This is certainly non-trivial.

Figure 2 shows good agreement between the estimates at distances farther "south" than -60 km and farther "north" than 30 km from the north wall of the Gulf Stream. The percentage difference between the estimates is not constant across the stream, implying that the difference is not due to a calibration error of the HEM. While there are many possible noises and small errors in the HEM data, none is known to result in an overestimate of velocity. We believe the error arises in the current meter data and/or its trapezoidal integration, but to date we have clearly identified only one source of error, which by itself, however, is insufficient to account for all of the error in Figure 2. Conductivity and temperature versus depth (CTD) data taken at this longitude by M. Hall indicate that the extrapolation of currents to the near-surface underestimates the upper ocean velocities (at and north of the maximum current) and the trapezoidal integration, which implies linear interpolation between 1000 and 3500 m, underestimates the transport

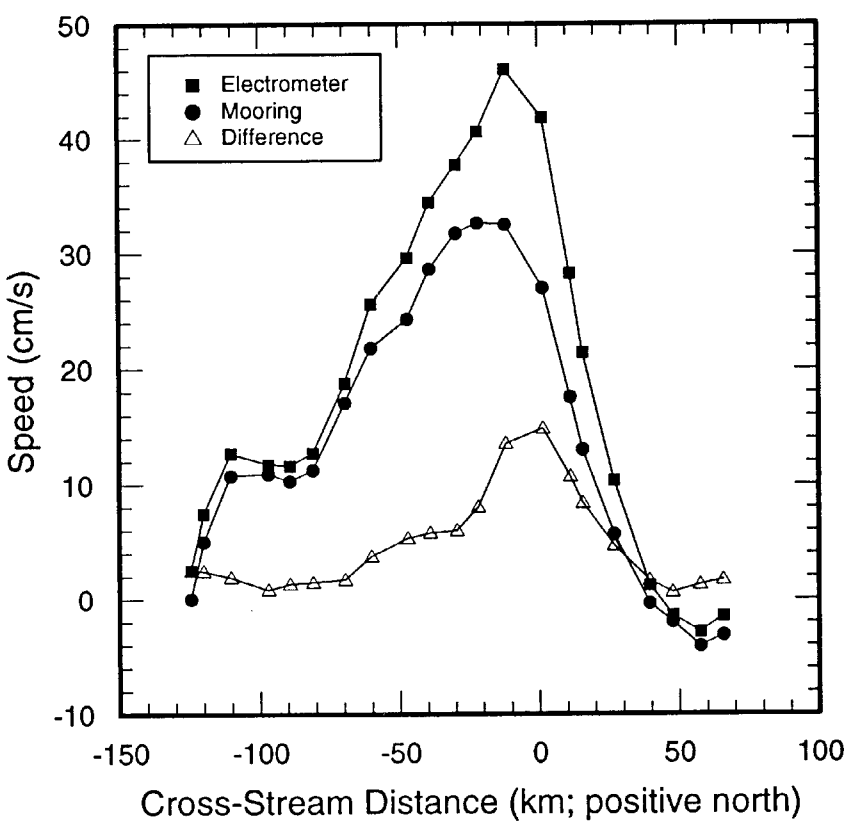

Figure 2. Two estimates of vertically averaged water velocity in the Gulf Stream at nominally 68°W, as a function of cross-stream distance, using electrometer and mooring data (see text). The differences between these estimates are also plotted.

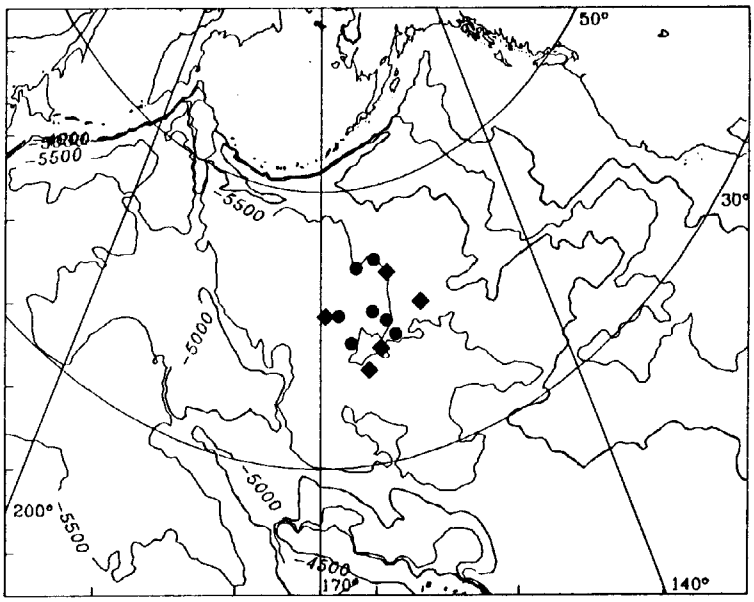

Figure 3. Polar stereographic projection of the North Pacific Ocean displaying seafloor isobaths from 4000 to 5500 m, and the locations of seafloor electrometers (solid circles) and pressure gauges during BEMPEX. Adjacent land masses are also shown.

between 1000 and 3500 m (again, at and north of the maximum current). Error from the trapezoidal integration is further suggested by the fact that the error time series is most highly coherent with currents measured at 1000 m.

Observation of Atmospheric Forcing of Sub-Inertial Gyre-Scale Eddies

A good example of the use of measurements of integrating variables to explore a phenomenon that defied unambiguous detection with traditional point measurements is the Barotropic, Electromagnetic and Pressure Experiment (BEMPEX). BEMPEX employed HEMs and bottom pressure gauges to specifically test theories (Frankignoul and Müller, 1979; Müller and Frankignoul, 1981) of stochastic forcing by the atmosphere of sub-inertial gyre-scale motions in the ocean. BEMPEX, fielded by ourselves with Jean Filloux and funded by the National Science Foundation, obtained seven HEF records and five bottom pressure records from a two-dimensional array spanning 1000 km centered around 40°N, 163°W (Figure 3) and lasting 11 months beginning in August, 1986. Luther et al. (1991) showed that the conductivity contribution (Eq. (5)) to the HEFs in BEMPEX was trivial, so that the HEFs were directly proportional to vertically averaged (barotropic) water velocity. In the following, we'll simply refer to the barotropic currents, rather than the HEFs, obtained from the HEMs.

Four of the observational strategies discussed in the introduction were employed in the design of BEMPEX: first, isolation, i.e., a region of the North Pacific was chosen for which it could be reasonably assumed that other sources of energy for gyre-scale motions (such as instabilities of strong "mean" currents) were weak; second, measurements of

integrating variables, HEFs and P_b, were planned, because the theories predicted that the oceanic response to atmospheric forcing would be essentially barotropic at the sub-inertial periods (i.e., a few days to a few months) that we could observe reasonably well with a one year record; third, a spatial array was planned for confirmation of theoretical predictions of frequency-wavenumber relations; and, fourth, visual and graphical comparisons with published model outputs of statistical parameters were planned. All these process discrimination strategies were employed because previous experiments had found that detection of atmospherically forced gyre-scale motions was difficult with traditional point measurements of currents and because the point measurements showed significant spatial inhomogeneities in what evidence of this phenomenon they did find. Figure 4 is presented as an example of how the integrating variable HEF readily provided evidence of atmospheric forcing, while at the same time measurements of currents in the surface mixed layer did not, probably because of the superposition of many phenomena in the mixed layer that have different, destructively interfering relationships with the surface atmospheric variables.

The Frankignoul and Müller papers listed above were the first papers to present the physics of atmospherically forced meso- and gyre-scale motions (which have the form of linear Rossby waves) in the realistic light of stochastic forcing; and, most important to empiricists, they presented testable hypotheses in the form of intervariable transfer and coherence functions. One example of the latter in flat-bottomed basins is the prediction of

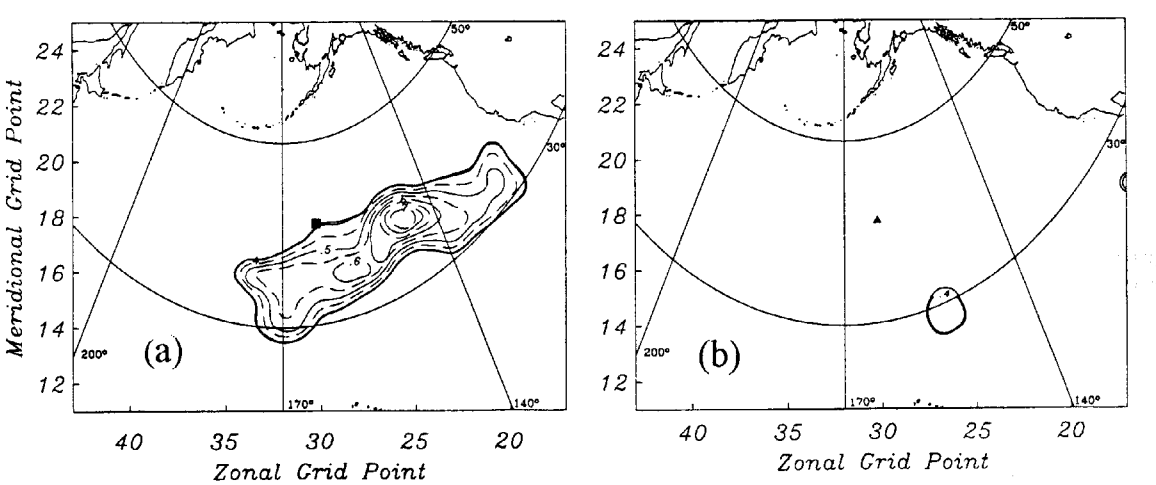

Figure 4. (a) Contour plot of squared coherence amplitude between BEMPEX zonal barotropic current (measured at the solid square) and surface zonal wind stress (at each grid point), in the 10-15 day period band. The wind stress was calculated (Chave et al., 1992b) from the Fleet Numerical Oceanography Center's surface wind product. Only squared coherence amplitudes greater than the 95% level of no significance are plotted. The large region of significant coherence indicates a strong relationship between oceanic barotropic (depth-independent) zonal current and atmospheric forcing. (b) As for (a), except with zonal current measured at nominally 73 m depth on a sub-surface mooring located near the electrometer in (a). The lack of significant coherence is interpreted as a null result, providing no information on the relatedness of oceanic near-surface zonal current and surface zonal winds.

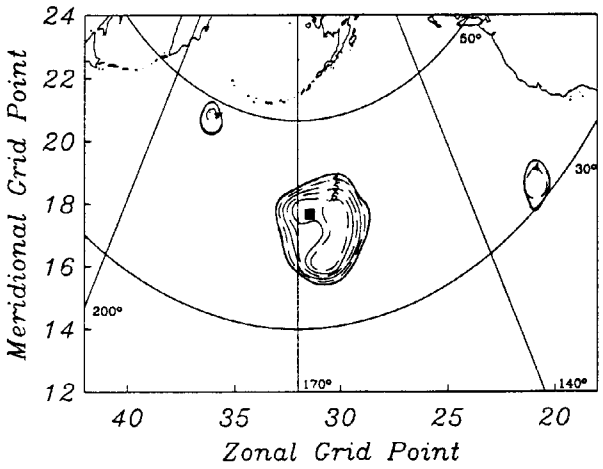

Figure 5. Contour plot of squared coherence amplitude between BEMPEX meridional barotropic current (measured at the solid square) and surface wind stress curl (at each grid point), in the 25-70 day band. Plotted as in Figure 4. The significant coherence surrounding the solid square suggests the oceanic meridional barotropic current is nearly in Sverdrup balance with the wind stress curl (see text). This is the only location (out of 7), and the only period band at this location, that exhibited a Sverdrup-like behavior.

strong coherence between meridional currents and local wind stress curl at periods greater than O(100 days). The coherence arises from the dominance of a "Sverdrup" balance in the vorticity conservation equation, in which the curl of the wind stress, which is a source of vorticity, is balanced by a meridional advection of planetary vorticity. The coherence does not occur at shorter periods due to destructive interference from many shorter scale waves with non-trivial relative vorticity. For basins with gently sloping bottoms, a "topographic Sverdrup" balance obtains between wind stress curl and oceanic currents that are perpendicular to isopleths of potential vorticity, f/H, where f is the Coriolis parameter.

Evidence for the flat-bottom Sverdrup relation was found in BEMPEX (Fig. 5), and evidence for the topographic Sverdrup relation was reported by Niiler and Koblinsky (1985). But, the coherence shown in Figure 5 did not occur at any other period for that instrument, nor was there Sverdrup-like coherence at any period for the other six HEMs. Furthermore, a systematic search of North Pacific current meter records by Koblinsky et al. (1989) produced no further examples of a topographic Sverdrup balance of oceanic currents. The problem lies with the generation of short-scale Rossby waves by short-scale topography as the wind stress curl drives the water across isopleths of f/H (Anderson and Corry, 1985; Cummins, 1991). The short-scale waves have substantial relative vorticity, so that a Sverdrup balance usually does not dominate vorticity conservation until very long periods. Cummins (1991) demonstrated, with a numerical model of the North Pacific having realistic topography, that by spatially filtering out the shorter scale waves the Sverdrup balance of the longer waves can be recovered. Following Cummins, we have averaged the meridional currents from the five HEMs that comprised a coherent sub-array in BEMPEX (Fig. 3). The resultant averaged meridional currents were coherent with wind stress curl at all periods >10 days; Figure 6 shows the coherences from two period bands.

BEMPEX yielded many significant statistics (Chave et al., 1992b) with which to determine the kinematics of the oceanic Rossby waves and with which to test Müller and

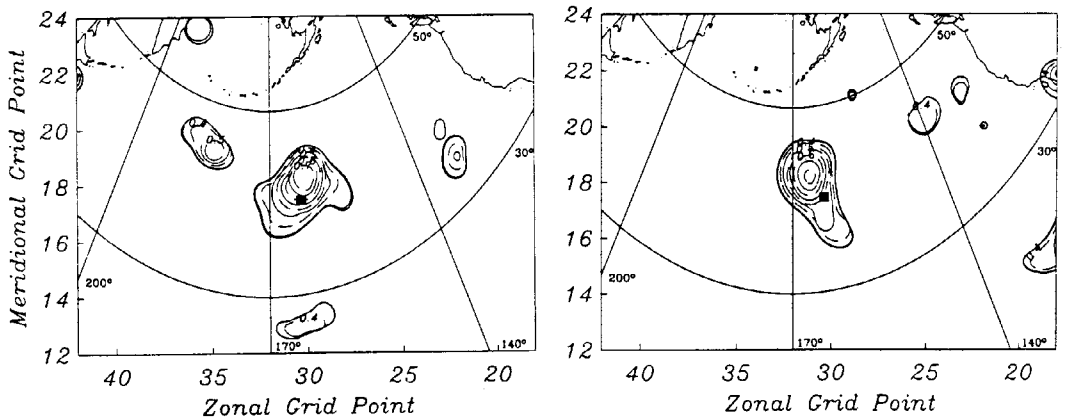

Figure 6. Contour plot of squared coherence amplitude between averaged BEMPEX meridional barotropic currents (measured at the 5 southernmost electrometers in Figure 3) and surface wind stress curl, in the (left) 25-70 day band, and (right) 13-19 day band. A Sverdrup-like relationship (see text) is evident in both period bands, and at all other periods greater than 10 days, for the averaged meridional barotropic current. The solid square in both plots locates the nominal center of mass of the five electrometers. Otherwise plotted as in Figure 4.

Frankignoul's (1981) predictions of frequency-dependent local coherence between various oceanic and atmospheric variables. Non-zero coherences between oceanic variables and non-local atmospheric variables, predicted by Brink (1989), were also unambiguously observed (Luther et al., 1990; Chave et al., 1992b). No point measurements of currents have yielded such clear evidence of direct atmospheric forcing of Rossby waves as has been obtained with measurements of the integrating variables, HEF and P_b (the latter to be discussed further below).

The example above, describing efforts to confirm the relatively simple physics inherent in the Sverdrup balance, emphasizes the non-homogeneity of even the larger scale barotropic motions in the ocean. Statistics estimated from observations of these phenomena are correspondingly inhomogeneous. Any observational program or statistical analysis technique, such as some of those highlighted at this workshop, must address these inhomogeneities or risk misdirected inferences.

BOTTOM PRESSURE (P_b)

The complete relationship between pressure and water velocity in the oceans is not easily represented by a simple integral. To lowest order, however, mid-latitude, sub-inertial motions are geostrophic, i.e.,

$$\bar{v}_h = \frac{1}{f\rho_s} k \times \nabla_h p, \tag{9a}$$

which permits the derivation of a simple relationship between pressure and the mass flux per unit vertical distance (Pedlosky, 1987), viz.,

$$p(\xi) = f \int_{\xi_0}^{\xi} k \cdot (\rho_s \vec{v}_h \times d\vec{r}) + p(\xi_0), \tag{9b}$$

where ξ and ξ_0 are two points in a horizontal plane; $d\vec{r}$ is an incremental vector parallel to an arbitary curve running from ξ_0 to ξ, so long as $p(\xi) > p(\xi_0)$; $\rho_s = \rho_* + \bar{\rho}(z)$; and k is the local upward unit vector.

Like HEFs, pressure is related to a spatial integral of horizontal velocity. Unlike HEFs, the spatial distance over which the integral operates is somewhat arbitrary for pressure. But, the greater the separation between members of a set of pressure measurements, the weaker the correlation between them due to the substantial wavenumber bandwidth of oceanic sub-inertial motions. Lack of coherence is usually fatal for process studies but is often considered irrelevant for basin-wide studies of transport, for instance. The integrating nature of pressure is in large part responsible for the successful mapping of the semi-permanent oceanic flows with hydrographic (temperature and salinity versus depth) data, from which pressure is calculated, because smaller scale variability tends to have a weaker impact on pressure (which can be argued from either Eq. (9a) or Eq. (9b)).

In addition to discriminating against smaller scales of motion, bottom pressure discriminates against baroclinic motions in favor of barotropic. This follows, for example, from the vertical structure functions, $\phi_i(z)$, that are determined from Eq. (6). The barotropic mode is independent of depth, while the baroclinic modes have their largest amplitudes near the sea surface. If the barotropic and baroclinic modes have identical total kinetic energy, integrated from the seafloor to the sea surface, then the barotropic mode will have a larger amplitude at the seafloor than any of the baroclinic modes. Since the barotropic and first baroclinic modes typically have similar kinetic energies (and the higher modes are weaker), P_b (but not pressure in the upper ocean) tends to be dominated by large-scale barotropic motions, even in regions of the oceans with energetic baroclinic mesoscale motions such as the western North Atlantic. This latter point accounts for the large horizontal correlation of sub-inertial P_b found over distances of hundreds of kilometers in the western North Atlantic by Brown et al. (1975) during the Mid-Ocean Dynamics Experiment, while horizontal correlations of currents and temperatures in the same general area tend to zero when separations of O(100 km) are attained (Owens, 1985).

Considering the tendency of P_b to be more or less dominated by the large-scale sub-inertial motions, we might expect that P_b in BEMPEX will be less affected by the short-scale waves that made detection of the Sverdrup balance, for instance, so difficult with point measurements of currents or even HEF-derived barotropic currents. In fact, we do find from BEMPEX that P_b is much more coherent with surface atmospheric variables (Fig. 7) than are the barotropic currents. And, the coherence between the pressure records is greater than found for the barotropic currents, despite the larger separation of the pressure gauges (Fig. 3). The extended regions of high squared coherence in Figure 7 are not so much evidence of waves reaching the instrument from all over the Pacific as they are evidence of high horizontal coherence in the surface atmospheric fields themselves. The non-local maximum of the squared coherence in Figure 7 is expected from the dominance of propagating waves over locally forced motions at these periods (Brink, 1989). As the period decreases, the maximum coherence between P_b and air pressure or wind stress curl becomes more local (Luther et al.,

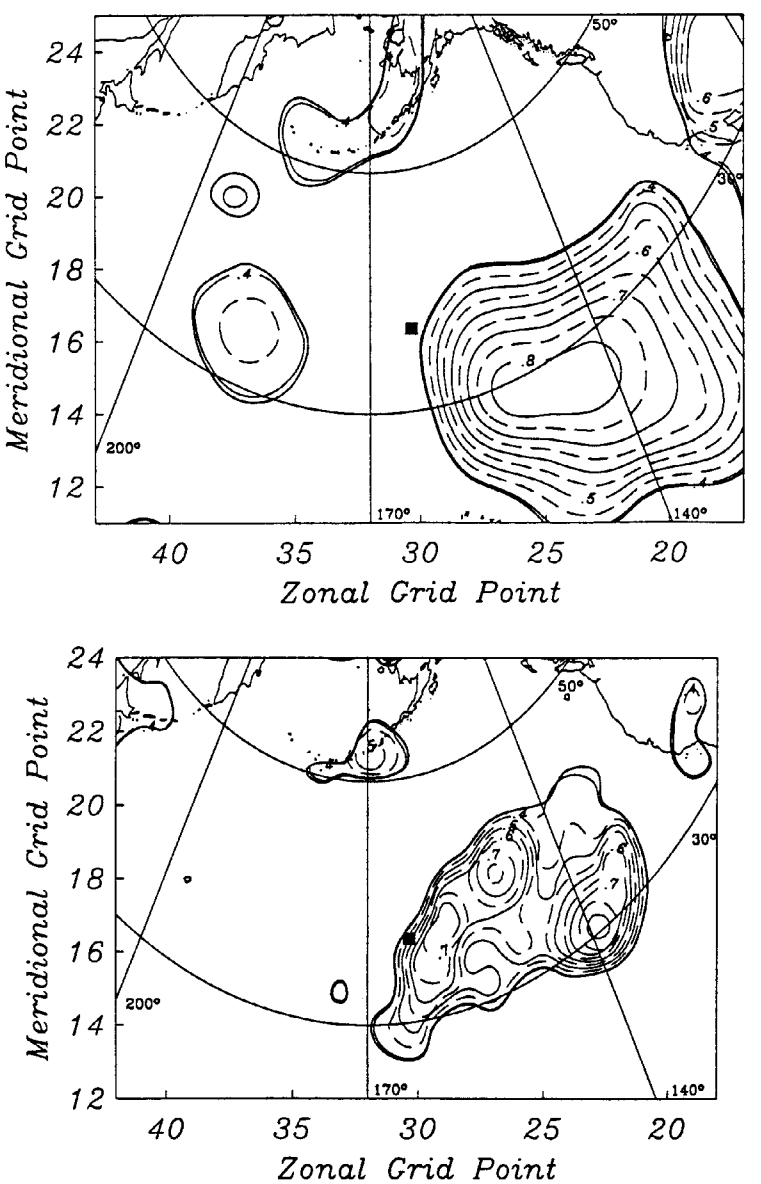

Figure 7. Contour plot of squared coherence amplitude between BEMPEX bottom pressure (measured at the solid square) and (top) surface air pressure, or (bottom) surface wind stress curl, both in the 19-38 day band. Plotted as in Figure 4. The extended regions of strong coherence are typical for the bottom pressure records at most periods, unlike the coherences found for barotropic currents which tended to be weaker, less extensive, more spatially inhomogeneous, and clearly significant in fewer period bands.

1990), in accordance with the disappearance of freely propagating Rossby waves (Müller and Frankignoul, 1981).

Bottom pressure P_b is so dominated by the larger scale barotropic motions that all the P_b records from BEMPEX display very similar coherence relationships with the atmospheric variables, unlike the situation for the barotropic currents which exhibit more inhomogeneities in their relationships with atmospheric variables. For P_b, atmospheric forcing is clear at all sub-inertial frequencies,as seen by the graphs of maximum coherence in Figure 8. The fact that the coherence of P_b with air pressure is frequently higher than its coherence with wind stress curl (Fig. 8) does not implicate a particular forcing mechanism, because the atmospheric variables are coherent among themselves, and there is more noise in wind stress curl than in air pressure. A simple scaling argument shows (Philander, 1978) that divergence of the surface (Ekman) boundary layer, produced by the curl of the wind stress, should dominate all other forcing mechanisms at the time and space scales observed in BEMPEX (Chave et al., 1992a).

COMBINING HEM AND IES MEASUREMENTS

The intent of this section is to demonstrate the great potential of combining measurements of two integrating variables listed in Table 1. The combination of measurements of horizontal electric fields (HEFs) and vertical acoustic travel times (VATTs) can provide estimates of (1) volume transport per unit width, (2) the gravest vertical structure (i.e., barotropic and first baroclinic modes) of the horizontal currents, and (3) the total heat flux (using the gravest vertical structures of the currents and temperature). Because seafloor HEMs and IESs are inexpensive to make and deploy compared to current meter moorings, it is not unreasonable to envision the deployment of large arrays of HEMs and IESs for both dynamical process studies and the accumulation of transport time series for climate studies. That most of the ocean's low frequency structure and variability can thereby be observed from the seafloor using integrating variables is quite remarkable.

The VATT measured by an IES is

$$\tau = 2\int_{-H}^{0} \frac{dz}{c}, \tag{10}$$

where H is the bottom profile, and $c = c(z,t)$ is the speed of sound. Potential small errors in the interpretation of VATT in terms of the simple relation in Eq. (10) have been enumerated by Watts and Rossby (1977).

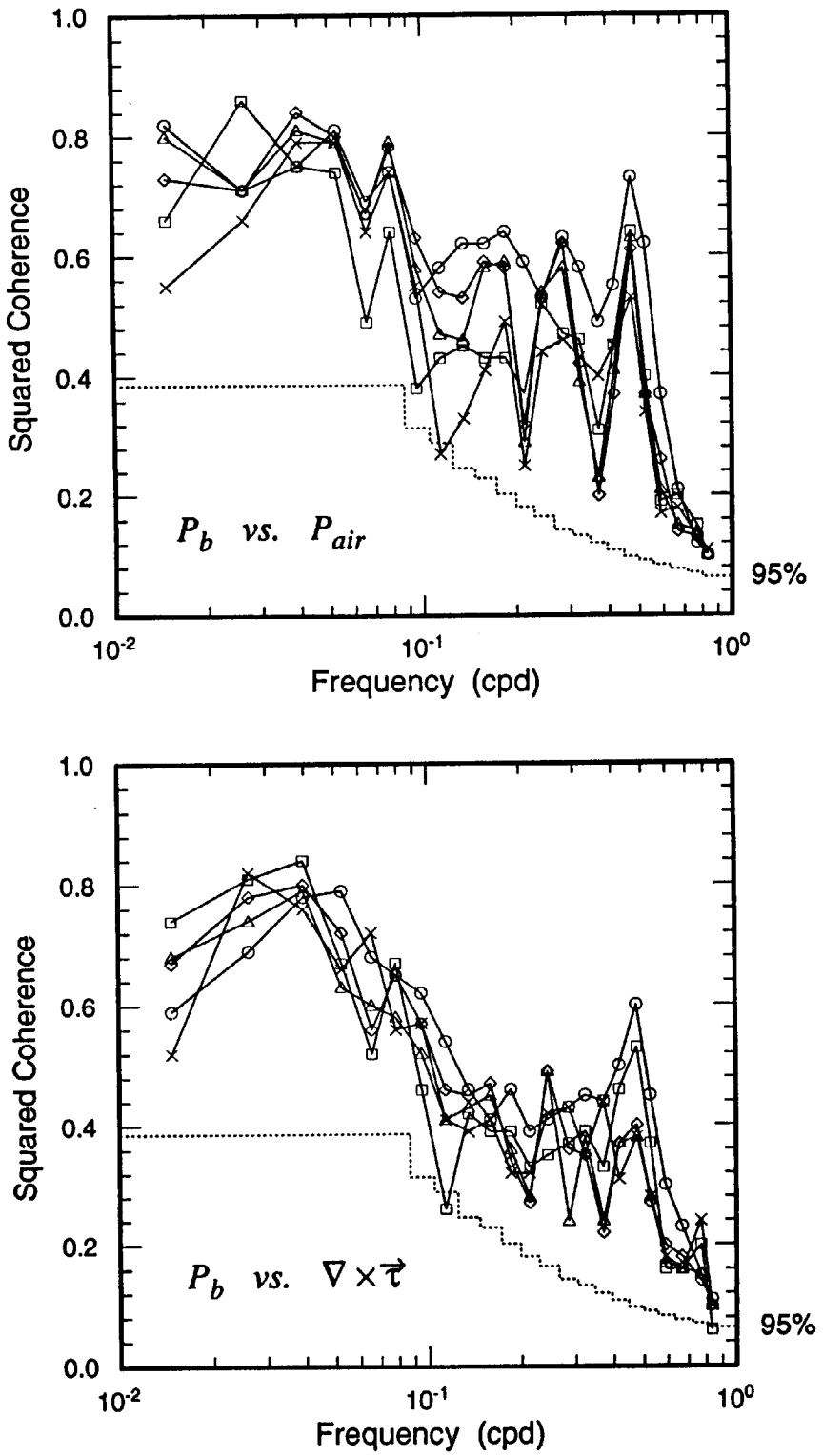

Figure 8. Maximum squared coherence amplitude, over the oceanic domain of Figure 3, between each BEMPEX bottom pressure record and (top) surface air pressure, or (bottom) surface wind stress curl, plotted as a function of frequency. The 95% level of no significance is indicated in each plot. For each station, every other point plotted is independent due to a 50% overlap of frequency band-averaging. The ubiquitously high coherence maxima indicate that bottom pressure, and hence the large-scale barotropic motions that it represents, is strongly related to atmospheric forcing in the central North Pacific.

First Baroclinic Displacement Mode Amplitude

Consider temperature, T, salinity, S, and pressure, P, as state variables, so $c(\vec{x},t) = c(T(\vec{x},t), S(\vec{x},t), P(\vec{x},t))$. Following Pickart and Watts (1990), we idealize variations in T and S as perturbations on a base profile which varies only with z (pressure is not perturbed since it is essentially the integration variable), therefore

$$T(z,t) = \overline{T}(z+\zeta(z,t)) \tag{11}$$

and similarly for S, where $|\zeta| << |z|$ by assumption. We now expand ζ in terms of displacement modes per Eq. (6), such that

$$\zeta(z,t) = \sum_{i=1}^{\infty} q_i(t)\, \theta_i(z), \tag{12}$$

where the q_i are non-dimensional since the θ_i have dimensions of length. Substituting Eq. (12) into the perturbation forms of T and S, and truncating after mode 1, the sound velocity can be written

$$c(z,t) = c\left[\overline{T}(z+q_1\theta_1), \overline{S}(z+q_1\theta_1), P(z)\right]. \tag{13}$$

After the basic state profiles are chosen, numerical evaluation of c based on its empirical dependence on T, S and P, using different values for q_1, leads to a functional relationship between τ and q_1 (Pickart and Watts, 1990), which can be inverted to yield the amplitude of the first baroclinic displacement mode for any measured VATT. In practice, since the depth is never known precisely enough, in situ profiles of T and S must be taken (by CTD or XBT) while the IES is deployed in order to calibrate the VATT. Pickart and Watts (1990) have shown evidence that the relationship between τ and q_1 in Eq. (13) is not sensitive to the choice of basic state profile of S (or buoyancy frequency, N, used in Eq. (6)), although they do note that the choice of basic state T profile is important, and a climatological mean T profile is inadequate in frontal regions such as the Gulf Stream.

The strong (weak) dependence of VATT on the first (other) baroclinic mode for mid-latitude hydrographic profiles has been documented by Watts and Rossby (1977) and Pickart and Watts (1990). (Also, Hall, 1986, and Pickart and Watts, 1990, have shown with current meter data that the first baroclinic mode dominates the vertical velocity, hence also the vertical displacement, in the Gulf Stream.) In the tropics, however, second baroclinic mode variability makes a non-trivial contribution to the VATT and cannot be ignored (Garzoli and Katz, 1981). In what follows, we are assuming the application is at mid- to high-latitudes.

First Baroclinic Current Mode Amplitude

Departing from previous authors, we develop an expression for the amplitude of the first baroclinic mode of current as follows. Under the hydrostatic and geostrophic approximations,

$$f\frac{\partial \vec{v}_h}{\partial z}=\frac{g}{\rho *}k\times\nabla_h\rho. \tag{14}$$

Let there be small perturbations of ρ as per Eq. (11), so that

$$\frac{\partial \vec{v}_h}{\partial z}=\frac{g}{f\rho_*}\frac{\mathrm{d}\bar{\rho}}{\mathrm{d}z}k\times\nabla_h\zeta. \tag{15}$$

Substituting the modal expansions for $\vec{v}_h$ and ζ (see Eqs. (6a) and (12)) in Eq. (15), applying the second relation in Eq. (6c), and truncating after mode 1 yields an expression for the amplitudes of the first baroclinic current modes, viz.,

$$\vec{a}_{h,1}=\frac{\gamma_1^2}{f}k\times\nabla_h q_1, \tag{16}$$

where γ_1^2 is the first baroclinic mode eigenvalue determined from Eq. (6). Note that none of the physical assumptions leading to Eq. (16), except the modal truncation, is more severe than is typically used to estimate relative or absolute (β spiral) currents from hydrographic data or to estimate cross-Gulf Stream profiles of current (and transport, after upward extrapolations) from single moorings (e.g., Hogg, 1992).

Analysis of the combined HEF and VATT datasets from the SYNOP experiment is in its early stages, but we can show a simple preliminary comparison of two derivations of one horizontal component of $\vec{a}_{h,1}$ in Figure 9a. Rather than using observed VATTs to estimate first mode displacement from Eq. (16), we simply assumed that the difference of the measured VATTs from two IESs is proportional to the first mode current amplitude, then estimated the constant of proportionality by least squares. The result is the dotted curve in Figure 9a. The solid curve in Figure 9a is an average of the first mode current amplitudes from three moorings, two at the endpoints, and one close to, the line running between the two IESs. The agreement between the curves is certainly encouraging.

Volume Transport Per Unit Width

Our estimate of volume transport per unit width is simply $\bar{a}_{h,0}$ from Eq. (8) times the depth, *H*. To solve Eq. (8), we need estimates of s_1 and $\bar{a}_{h,1}$. The latter are obtained from the IESs by Eq. (16). The former are obtained by reconstructing a time-dependent conductivity profile (using IES-derived estimates of q_1 in an expression for conductivity similar to that for sound speed in Eq. (13)), which is then decomposed according to Eq. (7).

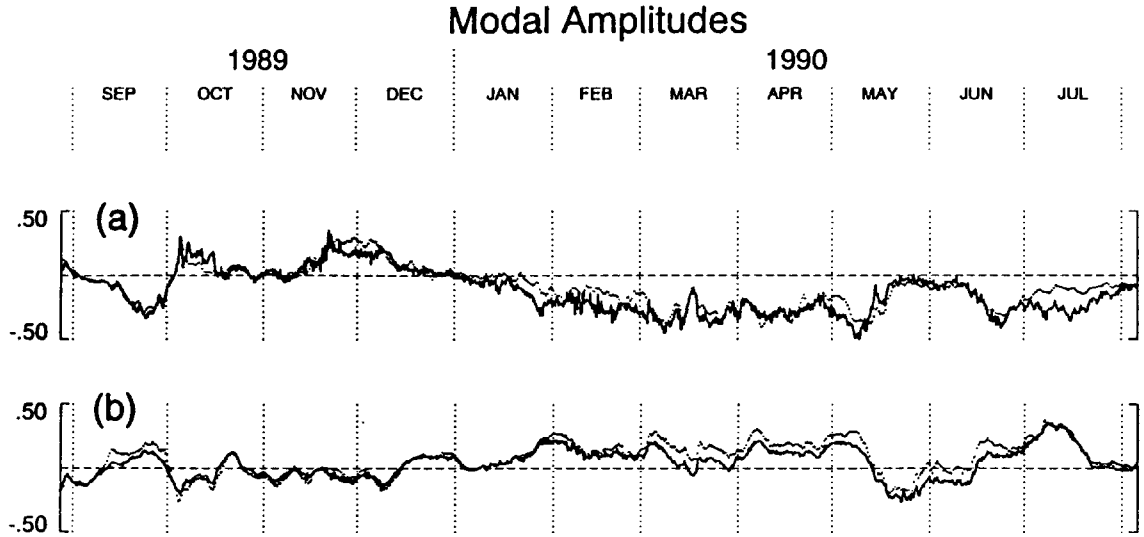

Figure 9. (a) IES (dotted curve) and mooring estimates (see text) of one component of the vector amplitude of the first baroclinic mode of horizontal current, $\vec{a}_{h,1}$. (b) HEM/IES (dotted curve) and mooring estimates (see text) of one component of the vector amplitude of the barotropic mode of horizontal current, $\vec{a}_{h,0}$. Data for both plots were taken during the SYNOP experiment in the Gulf Stream at nominally 68°W. Ordinate units are m/sec.

As in Figure 9a, a quick estimate of that component of $\vec{a}_{h,0}$ parallel to $\vec{a}_{h,1}$ shown in Figure 9a, is presented as the dotted curve in Figure 9b. The IES-derived estimate of $\vec{a}_{h,1}$ in Figure 9a was used in Eq. (8) with a climatological mean s_1. An average of the data from two HEMs (deployed near the IESs) was used in Eq. (8) as well. The only calibration employed was that for the first mode amplitude described above. The solid curve in Figure 9b is an average of barotropic mode current amplitudes from the same three moorings used in Figure 9a.

[Note that the comparison in Figure 9b is not directly relatable to the HEM-mooring comparison of transport estimates discussed previously, and evidenced by Figures 1 and 2, because Figure 9b only shows one of the two horizontal components of $\vec{a}_{h,0}$, and Figure 9b is necessarily derived from data spanning about 50 km, whereas the data for the prior comparison were all obtained at a single geographic location.]

Current Profiles and Heat Flux

The large vertical scale currents, $\vec{v}_h(z,t)$, are reconstructed by adding $\vec{a}_{h,0}$ and $\vec{a}_{h,1}\phi_1(z)$. The heat flux is readily obtained from this reconstructed current profile and a

reconstructed potential temperature profile, following Eqs. (11) and (12) truncated after mode 1.

Summary of Some Oceanic Variables Derivable from HEFs and VATTs

An ideal array would result in at least three IESs situated around each HEM. (Note that this does not mean that three times as many IESs are deployed as HEMs.) After choosing appropriate basic state temperature, $\overline{T}(z)$, and salinity, $\overline{S}(z)$, profiles, preferably from coincident CTD profiles rather than climatological mean profiles, the following are estimated:

$q_1(t)$, for each IES (see Eq. (13)) and subsequent discussion);

$\tilde{q}_1(t) = \frac{1}{m}\sum_{j=1}^{m} q_1^j(t)$, for the m IESs;

$\overline{T}_p(z)$, the basic state potential temperature profile, from the equations of state;

$T_p(z,t) = \overline{T}_p(z + \tilde{q}_1(t)\theta_1(z))$;

$\overline{\sigma}(z)$, the basic state conductivity profile, from the equations of state; and

$\sigma(z,t) = \overline{\sigma}(z + \tilde{q}_1(t)\theta_1(z))$.

Then the amplitudes of the first baroclinic modes of horizontal current are estimated from Eq. (16), viz.,

$$\vec{a}_{h,1} = \frac{\gamma_1^2}{f} k \times \nabla_h q_1,$$

where the eigenvalue γ_1^2 is obtained from solving Eq. (6) with a basic state buoyancy profile, $N^2(z)$, derived from the equations of state using $\overline{T}(z)$ and $\overline{S}(z)$. The barotropic modal amplitudes follow from Eq. 8, viz.,

$$a_{x,0} = \frac{E_{-y}^{u}(t)}{C|F_z|} - s_1 a_{x,1},$$

$$a_{y,0} = \frac{E_{x}^{v}(t)}{C|F_z|} - s_1 a_{y,1},$$

where s_1 is obtained from Eq. (7), using $\sigma(z,t)$ from above.

Finally, we arrive at estimates of the following oceanic quantities:

- Volume transport per unit width = $H\tilde{a}_{h,0}$;

- Horizontal current profiles, $\vec{v}_h(z,t) = \vec{a}_{h,0} + \vec{a}_{h,1}\phi_1(z)$; and

- Un-normalized heat transport per unit width = $\int_{-H}^{0} \rho_* C_p \vec{v}_h(z,t)\overline{T}_p(z,t)dz$,

where C_p is the specific heat of seawater at constant pressure.

CONCLUSIONS

The ability to observe variables (such as those listed in Table 1) that are natural spatial integrals of water motion or state properties in the oceans provides a useful, yet underutilized, strategy for process discrimination in field experiments. For those situations when observation of an integral quantity, like volume transport, is the desired end result, integrating variables are likely to yield more accurate results than point measurements of currents or state properties, as the one example presented above indicates. Integrating variables should also be more useful than point measurements for validation of numerical models of large-scale processes, because these variables in the ocean are not "contaminated" by short-scale processes that are not simulated in the models.

Specific estimation of statistics from integrating variables, examples of which were shown previously, demonstrate that even large-scale oceanic processes with the simplest physics exhibit significant spatial inhomogeneities. Any modelling effort, observational program, or statistical analysis technique, such as some of those highlighted at this workshop, must address these inhomogeneities or risk misdirected inferences.

Acknowledgments

The seventh 'Aha Huliko'a Hawaiian Winter Workshop on Statistical Methods in Physical Oceanography was an exceptionally stimulating meeting. We thank Peter Müller and Greg Holloway for designing and hosting the workshop, the Office of Naval Research for funding it, and Phyllis Haines for making sure it ran smoothly. Programming assistance from Jeff Bytof is gratefully acknowledged. Parts of the work presented here were supported by National Science Foundation Grant #OCE-8922948, Office of Naval Research Grant #N00014-90-J-1103, and National Oceanic and Atmospheric Administration Grant #NA16RC0545-01.

REFERENCES

Anderson, D.L.T. and R.A. Corry, 1985: Ocean response to low frequency wind forcing with application to the seasonal variation in the Florida Straits-Gulf Stream transport. *Prog. Oceanogr.*,14, 7-40.

Brink, K.H., 1989: Evidence for wind-driven current fluctuations in the western North Atlantic. *J. Geophys. Res.*, 94, 2029-2044.

Brown, W., W. Munk, F. Snodgrass, H. Mofjeld and B. Zetler, 1975: MODE bottom experiment. *J. Phys. Oceanogr.*, 5, 75-85.

Chao, B.F., 1988: Excitation of the Earth's polar motion due to mass variations in major hydrological reservoirs. *J. Geophys. Res.*, 93,13811-13819.

Chave, A.D., and D.S. Luther, 1990: Low-frequency, motionally induced electromagnetic fields in the ocean, 1, theory. *J. Geophys. Res.*, 95, 7185-7200.

Chave, A.D., D.S. Luther, and J.H. Filloux, 1992a: The Barotropic Electromagnetic and Pressure Experiment, 1. Atmospherically-forced barotropic currents, *J. Geophys. Res.*, 97, 9565-9593.

Chave, A.D., D.S. Luther, L.J. Lanzerotti and L.V. Medford, 1992b: Geoelectric field measurements on a planetary scale: Oceanic and geophysical applications. *Geophys. Res. Lett.*, 19, 1411-1414.

Chave, A.D., J.H. Filloux, D.S. Luther, L.K. Law, and A. White, 1989: Observations of motional electromagnetic fields during EMSLAB. *J. Geophys. Res.*, 94, 14153-14166.

Cronin, M., 1991: How good is the mooring motion correction? Tests using the Central Array current meter data. *SYNOPtician*, 2, 5-6 & 20-23.

Cummins, P.F., 1991: The barotropic response of the subpolar North Pacific to stochastic wind forcing. *J. Geophys. Res.*, 96, 8869-8880.

Eubanks, T.M., 1993: Variations in the orientation of the earth. American Geophysical Union Monograph: *Space Geodesy and Geodynamics*, in press.

Filloux, J.H., 1987: Instrumentation and experimental methods for oceanic studies. In: *New Volumes on Geomagnetism and Geoelectricity*, J. Jacobs (ed.), Academic Press, Chapter 3, pp. 143-247.

Frankignoul, C. and P. Müller, 1979: Quasi-geostrophic response of an infinite β-plane ocean to stochastic forcing by the atmosphere. *J. Phys. Oceanogr.*, 9, 104-127.

Garzoli, S., and E.J. Katz, 1981: Observations of inertia-gravity waves in the Atlantic from inverted echo sounders during FGGE. *J. Phys. Oceanogr.*, 11, 1463-1473.

Hall, M.M., 1986: Horizontal and vertical structure of the Gulf Stream velocity field at 68°W. *J. Phys. Oceanogr.*, 16, 1814-1828.

Hide, R. and J.O. Dickey, 1991: Earth's variable rotation. *Science*, 253, 629-637.

Hogg, N.G., 1991: Mooring motion revisited. *J. Atmos. Ocean. Technol.*, 8, 289-295.

Hogg, N.G., 1992: On the transport of the Gulf Stream between Cape Hatteras and the Grand Banks. *Deep-Sea Res.*, 39, 1231-1246.

Koblinsky, C.J., P.P. Niiler and W.J. Schmitz, Jr., 1989: Observations of wind-forced deep ocean currents in the North Pacific. *J. Geophys. Res.*, 94, 10773-10790.

Larsen, J.C., 1992: Transport and heat flux of the Florida Current at 27°N derived from cross-stream voltages and profiling data: theory and observations. *Phil. Trans. R. Soc. Lond. A*, 338, 169-236.

Larsen, J.C. and T.B. Sanford, 1985: Florida Current volume transport from voltage measurements. *Science*, 227, 302-304.

Levitus, S., 1982: *Climatological Atlas of the World Ocean*, NOAA Professional Paper #13, U.S. Government Printing Office, Washington, D.C.

Luther, D.S., Chave, A.D., J.H. Filloux, and P.F. Spain, 1990: Evidence for local and nonlocal barotropic responses to atmospheric forcing during BEMPEX. *Geophys. Res. Lett.*, 17, 949-952.

Luther, D.S., J.H. Filloux, and A.D. Chave, 1991: Low-frequency, motionally induced electromagnetic fields in the ocean, 2, Electric field and Eulerian current comparison from BEMPEX. *J. Geophys. Res.*, 96, 12797-12814.

Müller, P. and C. Frankignoul, 1981: Direct atmospheric forcing of geostrophic eddies. *J. Phys. Oceanogr.*, 11, 287-308.

Munk, W.H. and A.M.G. Forbes, 1989: Global ocean warming - An acoustic measure. *J. Phys. Oceanogr.*, 19, 1765-1778.

Niiler, P.P. and C.J. Koblinsky, 1985: A local time-dependent Sverdrup balance in the eastern North Pacific Ocean. *Science*, 229, 754-756.

Owens, B., 1985: A statistical description of the vertical and horizontal structure of eddy variability on the edge of the Gulf Stream recirculation. *J. Phys. Oceanogr.*, 15, 195-205.

Pedlosky, J., 1987: *Geophysical Fluid Dynamics*, 2nd Ed., Springer-Verlag, New York, 710 pp.

Pickart, R.S. and D.R. Watts, 1990: Using the Inverted Echo Sounder to measure vertical profiles of Gulf Stream temperature and geostrophic velocity. *J. Atmos. Ocean. Tech.*, 7, 146-156.

Philander, S.G.H., 1978: Forced oceanic waves. *Rev. Geophys. Space Phys.*, 16, 15-46.

Rossby, T., 1987: On the energetics of the Gulf Stream at 73W. *J. Mar. Res.*, 45, 59-82.

Sanford, T.B., 1971: Motionally-induced electric and magnetic fields in the sea. *J. Geophys. Res.*, 76, 3476-3492.

Sanford, T.B., 1986: Recent improvements in ocean current measurement from motional electric fields and currents. *Proc. IEEE Third Working Conf. on Current Measurement*, Airlie, Virginia, January 22-24, 1986, 65-76.

Sanford, T.B., R.G. Drever, and J.H. Dunlap, 1985: An acoustic Doppler and electromagnetic velocity profiler. *J. Atmos. Ocean. Technol.*, 2, 110-124.

Stephenson, D., and K. Bryan, 1992: Large-scale electric and magnetic fields generated by the oceans. *J. Geophys. Res.*, 97, 15467-15480.

Watts, D.R. and H.T. Rossby, 1977: Measuring dynamic heights with inverted echo sounders: Results from MODE. *J. Phys. Oceanogr.*, 7, 345-358.

Whitworth, T., III, and R.G. Peterson, 1985: The volume transport of the Antarctic Circumpolar Current from bottom pressure measurements. *J. Phys. Oceanogr.*, 15, 810-816.

Worcester, P.F., 1977: Reciprocal acoustic transmission in a midocean environment. *J. Acoust. Soc. Am.*, 62, 895-905.

Worcester, P.F., B. Dushaw and B. Howe, 1991: Gyre-scale reciprocal acoustic transmission. In: *Ocean Variability and Acoustic Propagation*, J. Potter and A. Warn-Varnas, Eds., Kluwer Academic Publishers, 119-134.